CRYSTAL GROWTH & DESIGN

Article

pubs.acs.org/crystal

Faceting of Equilibrium and Metastable Nanostructures: A Phase-Field Model of Surface Diffusion Tackling Realistic Shapes

Marco Salvalaglio,*[,†] Rainer Backofen,[‡] Roberto Bergamaschini,[†] Francesco Montalenti,*[,†] and Axel Voigt[‡]

[†]L-NESS and Dipartimento di Scienza dei Materiali, Università di Milano-Bicocca, Via R. Cozzi 55, 20125 Milano, Italy

[‡]Institut für Wissenschaftliches Rechnen, Technische Universität Dresden, 01062 Dresden, Germany

Supporting Information

ABSTRACT: Several crystalline structures are metastable or kinetically frozen out-of-equilibrium states in the phase space. When the corresponding lifetime is sufficiently long, typical equilibrium features such as regular and extended faceting can be observed. However, interpreting the extension of the facets and the overall shape in terms of a standard Wulff analysis is not justified. Here, we introduce a convenient general formulation of the anisotropic surface energy density, combined with a suitable phase-field model of surface diffusion. This allows for the investigation of the evolution toward equilibrium of realistically shaped nanostructures, describing an actual kinetic path and including the proper faceting. Numerical solution by the finite element method allows for efficient simulations even for the so-called *strong anisotropy* condition. After illustrating applications yielding equilibrium crystal shapes (corresponding to the Wulff construction), we focus our attention on faceting of structures in long-lived metastable states. The generality and numerical robustness of the approach is proven by a few applications to crystalline systems of great importance (quantum dots, quantum wires, patterned substrates) in present materials science.

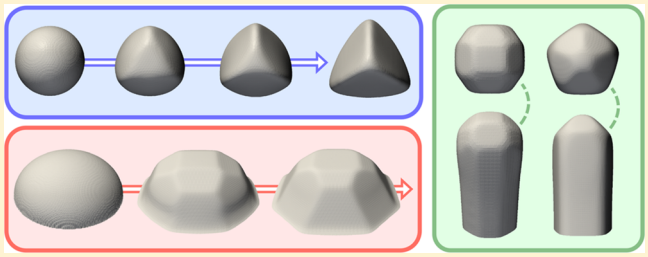

INTRODUCTION

The investigation of crystal morphologies is an interdisciplinary topic that plays an important role in the understanding of growth and processing of advanced crystalline materials. This applies, for instance, to metallic nanoparticles where shapes control can improve optical, electrical, and catalytic properties.[1−3] This is also observed for a large variety of semiconductor structures,[4−6] where the control of morphology and crystalline quality allows for the optimization of devices.[7] Moreover, crystal faceting and morphology-dependent properties are also interesting for organic compounds used, e.g., in molecular recognition and in medical applications.[8,9]

The observed crystal shapes are often interpreted in terms of surface energy minimization which implies the formation of facets corresponding to the minima in the surface energy density function $\gamma = \gamma(\hat{\mathbf{n}})$, where $\hat{\mathbf{n}}$ is the direction of the surface normal. The widely used Wulff construction[10,11] offers a simple method to determine the equilibrium crystal shape (ECS) with the constraint of a constant volume. This construction is identified as the convex hull of all the planes perpendicular to the $\mathbf{n}\hat{\gamma}(\hat{\mathbf{n}})$ vectors. Several numerical implementations of this procedure are available in the literature[12−14] allowing the ECS corresponding to a given $\gamma(\hat{\mathbf{n}})$ to be effectively depicted. Such a description is appropriate when considering homogeneous systems close to the thermodynamic equilibrium, while it generally does not hold when considering far-from-equilibrium conditions.[15] If the crystal evolution is fully dominated by kinetics, facet velocities $v(\hat{\mathbf{n}})$ can be considered in place of $\gamma(\hat{\mathbf{n}})$, and a *kinetic* Wulff construction can still be used in order to predict the crystal morphology.[16−18] Here we are interested in the regime where the system tends to minimize free energy, but kinetics poses constraints on the actual evolution, and/or the initial morphology leads to a local free-energy minimum.

A continuum model of surface diffusion, driven by the tendency to minimize the surface area, was already proposed in the 50s by Mullins[19] and further extended in order to include the effects of anisotropic $\gamma(\hat{\mathbf{n}})$.[20,21] Its advantage mainly consists in providing a kinetic path for the evolution toward equilibrium, including all the intermediate stages. Unlike the morphology given by the ECS, which is uniquely determined by $\gamma(\hat{\mathbf{n}})$, this approach may predict different final configurations, depending on the initial geometry.

However, the implementation of surface diffusion simulations including anisotropic surface energy is far from trivial. One of the most relevant issues is due to the stiffness of the corresponding partial differential equation (PDE) system. In particular, this is critical in the so-called *strong anisotropy* regime, when deep minima are present in $\gamma(\hat{\mathbf{n}})$ producing missing orientations and sharp corners in the ECS.[22−24]

Received: February 4, 2015
Revised: April 16, 2015
Published: April 22, 2015

DOI: 10.1021/acs.cgd.5b00165
Cryst. Growth Des. 2015, 15, 2787−2794

Another limit in describing realistic structures consists of the representation and tracking of the surface profile. In this respect, level-set or phase-field (PF) approaches take advantage of the implicit description of the geometry, allowing researchers to easily manage three-dimensional (3D) domains and complex topologies eventually changing in time.[21] Several applications of PF methods to the study of anisotropic systems are available in the literature (see ref 21 for a review). However, in most cases, only simplified $\gamma(\hat{\mathbf{n}})$ are considered with no claim on describing the complexity of realistic morphologies.

In the present work we introduce a convenient form for $\gamma(\hat{\mathbf{n}})$ within a suitable PF model of surface diffusion. The finite element method (FEM) toolbox AMDiS,[25,26] optimized for PF, was used. This way, we are able to provide a description of the evolution of 3D morphologies with an arbitrary faceting resulting from the choice of $\gamma(\hat{\mathbf{n}})$, even in the cases of strong anisotropy. As we shall show, this description is fully consistent with the standard Wulff approach when considering equilibrium conditions leading to the expected ECS. Furthermore, time evolution including major changes in faceting can be readily tackled, thus allowing for a proper description of metastable or out-of-equilibrium states. The efficacy of our approach in reproducing realistic structures is proved by comparing simulation results with experimental morphologies found in the literature.

MODEL DESCRIPTION

In order to reproduce the surface morphology of 3D geometries and their time evolution, we consider a diffuse-interface approach[21] based on a PF model of surface diffusion including surface energy anisotropy as proposed by Torabi et al. in ref 27. Within such a framework the profile evolution is implicitly tracked by considering an auxiliary analytic function φ, i.e., the phase field, smoothly varying from $\varphi = 1$ in the solid phase to $\varphi = 0$ in the vacuum. Its expression is given by

$$\varphi = \frac{1}{2}\left[1 - \tanh\left(\frac{3d(\mathbf{r})}{\epsilon}\right)\right] \tag{1}$$

where ϵ is the interface width and $d(\mathbf{r})$ is the signed distance from the (sharp) interface profile (nominally corresponding to the $\varphi = 0.5$ iso-surface) which consists of the surface of the solid phase. Figure 1 shows a spherical shape defined implicitly by means of φ, embedded in a $\varphi = 0$ domain, i.e., the vacuum, which is chosen cubic in shape. Every geometrical property of the surface can be derived directly from φ. In particular, the outer surface normal, which defines the local surface orientation, is $\hat{\mathbf{n}} = -\nabla\varphi/|\nabla\varphi|$.

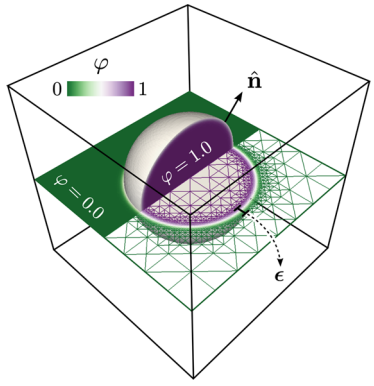

Figure 1. Illustrative scheme of an implicit sphere definition by means of φ. The spherical shape is embedded in the simulation domain (a simple cube), whose outline is shown in a perspective view. A slice of the simulation domain reveals its relative size with respect to the sphere and the refined mesh grid when $\varphi \approx 0.5$.

In order to consider an equation for the dynamics of φ, we introduce the surface energy F_s as given by the Ginzburg–Landau energy functional,[21,28]

$$F_s[\varphi] = \int_\Omega \gamma(\hat{\mathbf{n}})\left(\frac{\epsilon}{2}|\nabla\varphi|^2 + \frac{1}{\epsilon}B(\varphi)\right) d\mathbf{r} \tag{2}$$

with $B(\varphi) = 18\varphi^2(1-\varphi)^2$, i.e., the double well potential which promotes the state $\varphi = 0$ and $\varphi = 1$. According to the Onsager linear law, material flow is driven by the gradient of the local chemical potential μ, i.e., the variational derivative of eq 2:

$$\mu = \mu_s = \frac{\delta F_s}{\delta\varphi} \approx -\epsilon\nabla\cdot[\gamma(\hat{\mathbf{n}})\nabla\varphi] + \frac{1}{\epsilon}\gamma(\hat{\mathbf{n}})B'(\varphi) + -\epsilon\nabla\cdot[|\nabla\varphi|^2\nabla_{\nabla\varphi}\gamma(\hat{\mathbf{n}})] \tag{3}$$

where in the last term we used the asymptotic limit $(1/\epsilon)B(\varphi) \to (\epsilon/2)|\nabla\varphi|^2$ for $\epsilon \to 0$ and $\nabla_{\nabla\varphi}$ is the gradient which takes effect along the $\nabla\varphi$ direction. This definition of μ corresponds to the well-known Gibbs–Thomson chemical potential.[15] The profile evolution is then defined by tracking the changes of φ according to the continuity law

$$\frac{\partial\varphi}{\partial t} = \nabla\cdot[M(\varphi)\nabla\mu] \tag{4}$$

where the mobility function is set as $M(\varphi) = D(36/\epsilon)\varphi^2(1-\varphi)^2$ to restrict the diffusion at the surface, and D sets the time scale of the evolution. The dynamics described by eq 3 is well-posed only for weak anisotropy.

If $\gamma(\mathbf{n})$ yields to strong anisotropy, the so-called Willmore regularization[27,29] must be included in the free energy definition as an additional term F_{reg}, approximating the integral of the squared local curvature:

$$F_{reg} = \frac{\beta}{2\epsilon}\int_\Omega\left(-\epsilon\nabla^2\varphi + \frac{1}{\epsilon}B'(\varphi)\right)^2 d\mathbf{r} \tag{5}$$

Such regularization is a penalizing term which increases the energy of high curvature regions, healing the expected instabilities in the surface diffusion. Its effect on the morphology consists of a rounding of the corners controlled by the β parameter. From a physical point of view, this term can also be interpreted as an edge/corner energy.[22] In the presence of the regularization, μ must include also a $\delta F_{reg}/\delta\varphi$ term leading to

$$\mu = \mu_s + \beta\left(-\nabla^2\kappa + \frac{1}{\epsilon^2}B''(\varphi)\kappa\right) \tag{6}$$

where μ_s is given by eq 3 and $\kappa = -\epsilon\nabla^2\varphi + (1/\epsilon)B'(\varphi)$. Notice that, when including the regularization, a 6th order PDE has to be solved. This is quite demanding from a numerical point of view, and accurate space and time discretization is required. The FEM toolbox AMDiS,[25,26] used in the present work, allows one to efficiently manage the numerical integration of the reported equations. In fact, space adaptivity is built-in, allowing for a fine spatial resolution at the interface where φ varies significantly and the surface diffusion is active (see Figure 1). This ensures describing the interface region with a good

DOI: 10.1021/acs.cgd.5b00165
Cryst. Growth Des. 2015, 15, 2787–2794

enough accuracy while coarser resolution is used in the bulk region, reducing the computational cost. Time adaptivity has been also exploited to optimize the evolution time steps on the basis of the maximum variation of the profile. Zero-flux Neumann BCs are set at all the domain boundaries (faces of the cubic box in Figure 1). For the sake of simplicity, in the following the unit of length is dimensionless while the time scale is given in $1/(\gamma_0 D)$ units by setting γ_0 and D equal to 1. The details about the integration scheme are reported in the Supporting Information.

Surface Energy Density: A Convenient form. A fully customizable formulation for the $\gamma(\hat{\mathbf{n}})$ function is here introduced in order to account for the complexity of realistic morphologies. The key point for such a function is to quantify the difference between the local surface orientation $\hat{\mathbf{n}}$ and the vectors which give minima in the surface energy density ($\hat{\mathbf{m}}_i$).[30] This is achieved by considering the scalar product $\hat{\mathbf{n}}\cdot\hat{\mathbf{m}}_i$. Then the surface energy can be parametrized as

$$\gamma(\hat{\mathbf{n}}) = \gamma_0\left(1 - \sum_i^N \alpha_i\left(\hat{\mathbf{n}}\cdot\hat{\mathbf{m}}\right)^{w_i}\Theta(\hat{\mathbf{n}}\cdot\hat{\mathbf{m}})\right) \tag{7}$$

where N is the total number of energy minima. α_i and w_i are positive coefficients setting the depth and the width of the minima, respectively. $w_i \geq 2$ is required for differentiability. The Heaviside step function Θ is introduced in order to exclude energy contributions when the component of $\hat{\mathbf{n}}$ along the $\hat{\mathbf{m}}_i$ direction is negative. This allows us to control $\pm\,\hat{\mathbf{m}}_i$ facets independently. The role of each term in the summation of eq 7 can be easily seen by considering how $\gamma(\hat{\mathbf{n}})$ behaves in the presence of a single minimum along the $\hat{\mathbf{m}}$ direction. It is equal to $\gamma_0(1-\alpha)$ if $\hat{\mathbf{n}} \equiv \hat{\mathbf{m}}$, and it increases up to γ_0 moving away from $\hat{\mathbf{m}}$. It is worth to mention that our definition permits us to recover some typical $\gamma(\hat{\mathbf{n}})$ functions used in the literature. In particular, cubic symmetry resulting from $\gamma(\hat{\mathbf{n}}) = \gamma_0\,[1 + \tilde{\alpha}\,(n_x^4 + n_y^4 + n_z^4)\,]$,[27,31] can be obtained from eq 7 by considering the six minima along the orthogonal axes $\hat{\mathbf{m}}_{1,2} = [\pm 1\ 0\ 0]$, $\hat{\mathbf{m}}_{3,4} = [0\ \pm 1\ 0]$, $\hat{\mathbf{m}}_{5,6} = [0\ 0\ \pm 1]$, with $w_i = 4$ and constant α_i for each minimum.

In Figure 2a–c some illustrative 2D surface energy density functions $\gamma(\theta)$ (with $\theta = -\arctan(n_y/n_x)$ the angle between the normal vector and the [10] direction) are reported. In particular, a case with minima at $\overline{\theta}_i = i\,\pi/4$ with $i \in \mathbb{Z}$ (i.e., ⟨10⟩ and ⟨11⟩ directions) is considered. In Figure 2a we show the curves obtained with three different values of w_i but the same α_i. Notice that the width of the energy minima is inversely proportional to w_i. Moreover, when $w_i = 8$ a significant superposition of different contributions in the summation of eq 7 is seen for all orientations, and $\gamma(\overline{\theta}_i)$ results lower than $\gamma_0(1-\alpha_i)$. Increasing w_i (see $w_i = 20$ curve), no effective superposition takes place at $\theta = \overline{\theta}_i$, but it still occurs for orientations in between. For large enough w_i (see $w_i = 100$ curve), a full decoupling of the energy minima is achieved and orientations with $\gamma(\theta) = \gamma_0$ appear. Features of eq 7 can be also controlled in order to localize a single minimum, as required in order to tune independently the energy value corresponding to the minima orientations, i.e., the energy of the facets. This is shown in Figure 2b, where the same curves reported in panel a are considered with w_0 (width parameter for the $\overline{\theta}_0$ minimum) increased by a factor 10. Furthermore, we can enhance the stability of the $\theta = \overline{\theta}_0$ orientation, by setting a deeper minimum with higher α_i, as shown in Figure 2c. Similar arguments hold also when three-dimensional $\gamma(\hat{\mathbf{n}})$ functions are considered. In

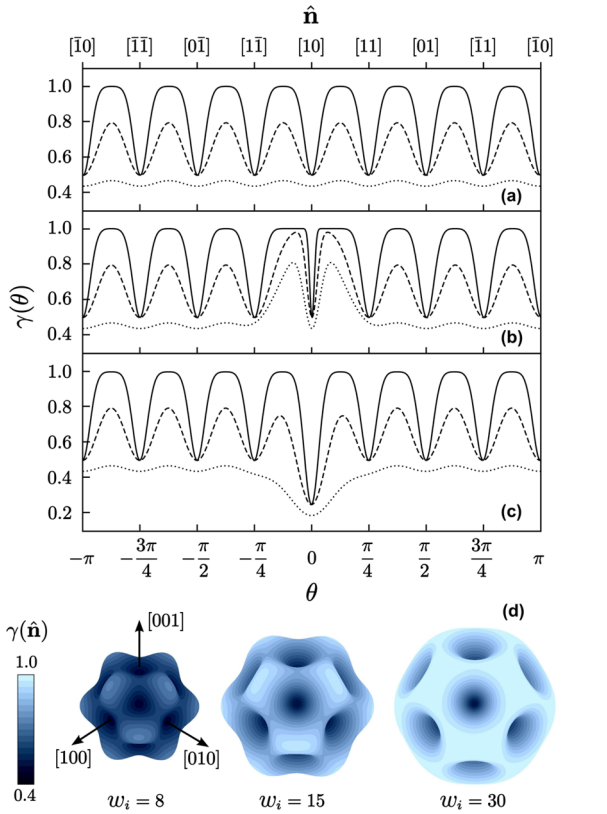

Figure 2. Examples of surface energy density from eq 7. (a–c) Plot of 2D $\gamma(\theta)$ function with minima at $\overline{\theta}_i = i\pi/4$ (⟨10⟩ and ⟨11⟩ directions) with $\alpha_i = 0.5$ and $\gamma_0 = 1$. (a) $w_i = 8$ (dotted line), $w_i = 20$ (dashed line), and $w_i = 100$ (solid line). (b) as in panel (a) with w_0 increased by a factor 10. (c) as in panel (a) with $\alpha = 0.75$ for the $\overline{\theta}_0$ minimum. (d) Three-dimensional $\gamma(\hat{\mathbf{n}})$-plot with minima along ⟨100⟩ and ⟨111⟩ directions, $\alpha_i = 0.5$ and $\gamma_0 = 1$, for three w_i values. $\gamma(\hat{\mathbf{n}})$ values are also plotted as surface color map.

this case the superposition of the minima contribution can be more complex, but the qualitative behavior of the 2D case is recognized. In Figure 2d, some $\gamma(\hat{\mathbf{n}})$-plots are shown for minima along ⟨100⟩ and ⟨111⟩ directions, $\alpha_i = 0.5$ and three different w_i values. The color map reveals the superposition and decoupling effects observed by increasing w_i value. From a general point of view, eq 7 can then be considered as a convenient way to construct a continuum $\gamma(\hat{\mathbf{n}})$ from discrete values corresponding to energy minima.

With an arbitrary choice of eq 7 parameters, $\gamma(\hat{\mathbf{n}})$ can become nonconvex (strong anisotropy), thus requiring the regularization introduced in eq 5. A remarkable analytic criterion has been developed in ref 31 in order to determine if missing orientations occur in the ECS for a given $\gamma(\hat{\mathbf{n}})$. This consists in evaluating when the product of the two Gaussian curvatures K_1K_2 of the $1/\gamma$-plot is negative. We used this criterion in order to determine *a priori* what is the expected regime related to the choice of the $\gamma(\hat{\mathbf{n}})$ parameters. For a single minimum direction we evaluated the critical α coefficient as a function of the w value, by numerically solving the $K_1K_2 = 0$ condition (see Supporting Information for the explicit formulas). The resulting curve is shown in Figure 3 and it is well reproduced by

$$\alpha_c(w) = \frac{A}{w} + \frac{B}{w^2} \tag{8}$$

DOI: 10.1021/acs.cgd.5b00165
Cryst. Growth Des. 2015, 15, 2787–2794

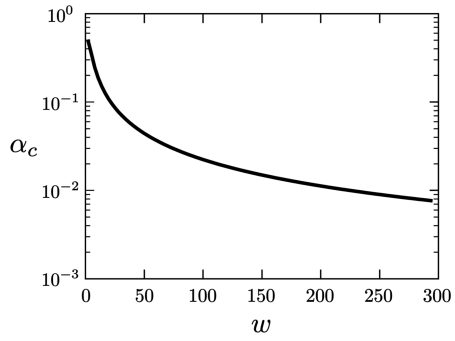

Figure 3. Critical α values as a function of w obtained by numerically solving $K_1K_2 = 0$ for a $\gamma(\hat{\mathbf{n}})$ defined by eq 7 with a single minimum orientation.

where $A = 2.26 \pm 0.2\%$ and $B = -2.48 \pm 0.4\%$ deliver the best fit. If minima contribution in eq 7 are decoupled, one can directly assess what is the anisotropy regime only by comparing the α_i values with the data in Figure 3 or with eq 8. Conversely, if minima contributions are superimposed for some orientations, the explicit numerical evaluation of K_1K_2 is required in order to determine the anisotropy regime and the critical parameters.

RESULTS AND DISCUSSION

Evolution from a Sphere toward the Equilibrium Crystal Shape. As a first case study, we focus on obtaining the ECS as the stationary state delivered by surface diffusion simulations via the aforementioned PF model. Furthermore, we inspect the customization of the final geometry by suitable choices of the $\gamma(\hat{\mathbf{n}})$ in eq 7, tuning its parameters as well as the strength of the Willmore regularization β. We consider a sphere of radius 0.3 as initial profile, implicitly defined into the integration domain, set as a cubic box with lateral size equal to 1, as shown in Figure 1. The interface width ϵ is arbitrarily set equal to 0.04, in order to ensure an appropriate resolution of the surface profile on the mesh. The profile evolution is then obtained by integrating the surface diffusion equation for φ. The local material transport, driven by $\nabla\mu$, finally leads to a stable faceted shape which corresponds to the ECS.

Figure 4 provides some examples of simulation results obtained starting from a spherical profile and evolving toward equilibrium according to eq 4, for different definitions of $\gamma(\hat{\mathbf{n}})$. In Figure 4a we consider minima directions corresponding to the facet orientations of a tetrahedron. This shape does not have an inversion center, and we select it to demonstrate the possibility to obtain single facets without symmetry requirements. As made evident by the evolution sequence, facets are gradually formed from the initial spherical profile leading to the expected polyhedron as an equilibrium condition. In Figure 4b a different $\gamma(\hat{\mathbf{n}})$ with two different families of minima directions, along $\langle 100\rangle$ and $\langle 111\rangle$ is considered, and the resulting ECS is shown. In Figure 4c the actual faceting of the final geometries reported in Figure 4a,b is highlighted by showing $\gamma(\hat{\mathbf{n}})$ as a color map at the surface. The large regions in uniform (blue) color correspond to almost flat facets oriented according to the minima in $\gamma(\hat{\mathbf{n}})$. Edges and corners in between, which smoothly connect facets, have intermediate orientations with higher energy values.

By tuning the parameters of eq 7, we can modify also the features of the equilibrium shape for a given set of minimum directions. Figure 5a shows the ECS obtained with the same

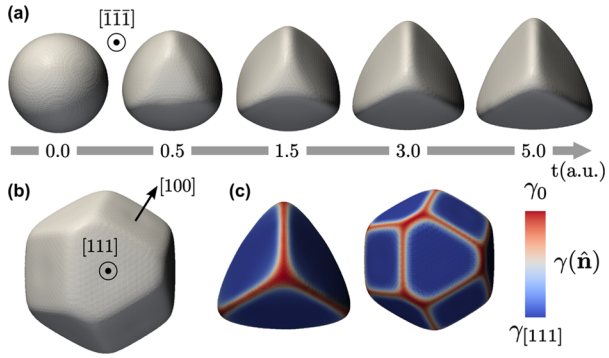

Figure 4. Surface diffusion evolution toward the ECS. (a) From a sphere to a tetrahedron with minima of $\gamma(\hat{\mathbf{n}})$ along $[\bar{1}\ \bar{1}\ 1]$, $[\bar{1}\ 1\ \bar{1}]$, $[1\ \bar{1}\ \bar{1}]$, and $[1\ 1\ 1]$ directions with $\alpha_i = 1.0$, $w_i = 6$, $\beta = 0.002$. (b) ECS simulated by considering minima along the $\langle 100\rangle$ and $\langle 111\rangle$ directions with $\alpha_i = 0.3$, $w_i = 20$ and $\beta = 0.001$. (c) Color map, scaled by the $\gamma_{[111]}$ value, showing the $\gamma(\hat{\mathbf{n}})$ for the geometries shown in (a) and (b), respectively.

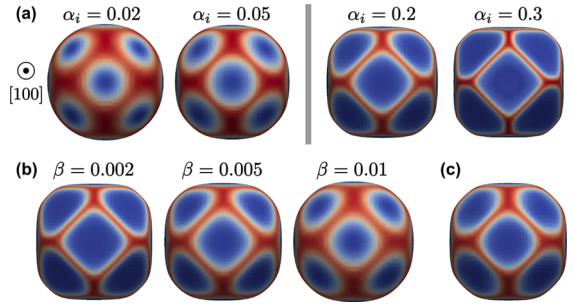

Figure 5. Dependance of ECS on (a) α_i, both in weak (left) and strong (right) anisotropy regime, (b) β values, (c) the radius of the initial sphere, here considered doubled with respect to the one in panel (b) with $\beta = 0.01$. Minimum directions are set as in Figure 4b. $\gamma(\hat{\mathbf{n}})$ color map is shown as in Figure 4c.

$\gamma(\hat{\mathbf{n}})$ used in Figure 4b with different anisotropy degrees, i.e., with different α_i values. Both weak and strong anisotropy conditions are considered. Notice that, even for weak anisotropy, preferential orientations are present but with rather large angular dispersion around minima so that an almost rounded geometry is obtained. The selectivity on the minima orientation increases for larger α_i leading to more defined facets. As a result, the stronger the anisotropy, the more contracted are the (red) areas with high $\gamma(\hat{\mathbf{n}})$ between the facets. It must be noticed that, due to the continuum description of the profile, such rounded edges/corners cannot be avoided. Polyhedron-like structures can then be obtained only by restricting such regions as much as possible by increasing α. However, when entering the strong anisotropy regime, the Willmore regularization term introduces an additional driving force toward rounding, depending on the parameter β. The same $\gamma(\hat{\mathbf{n}})$ used in Figure 4b has been considered in Figure 5b, by setting different β values. We notice that the larger its value the more extended is the rounded area between the different facets.[22,25] Furthermore, the effect is more dramatic at the corners than at the edges, as the local curvature is larger. In order to obtain sharper facets, for a given set of $\gamma(\hat{\mathbf{n}})$ parameters, one should then lower β as much as possible. However, the lowest value which can be used for such a parameter depends in general on the interface width and on the spatial discretization of the FEM method. A trade-off

DOI: 10.1021/acs.cgd.5b00165
Cryst. Growth Des. 2015, 15, 2787−2794

between the need to obtain sharp facets and the computational cost is thus required. It must also be pointed out that, at variance from the $\gamma(\hat{\mathbf{n}})$ contribution yielding self-similar geometries when rescaling the crystal volume, the Willmore regularization is set on an absolute length scale since β directly defines the rounding radius, independently of the facets extension.[25] This is illustrated in Figure 5c where the radius of the crystal is doubled, while using the same $\gamma(\hat{\mathbf{n}})$ of Figure 5b with $\beta = 0.01$. The relative extensions of the rounded regions at the edges are more localized, thus the shape looks more similar to the case with lower β values, i.e., sharper facets are obtained.

More complex geometries can also be reproduced since our definition of $\gamma(\hat{\mathbf{n}})$ does not rely on any imposed symmetry in the surface energy, as shown with few examples in Figure 6. In particular, Figure 6a illustrates the effect of setting different energy values for the minima in $\gamma(\hat{\mathbf{n}})$. The same parameters of Figure 4b are considered but α_i corresponding to the minima along ⟨111⟩ directions are lowered by a factor 2. As expected, the resulting ECS exhibits much larger {1 0 0} facets, thanks to their enhanced stability. Examples of more complex, asymmetric ECS are shown in Figure 6b,c. From the reported results we conclude that within our PF approach we can control the ECS features, eventually matching the standard Wulff construction in the limit $\beta \to 0$.

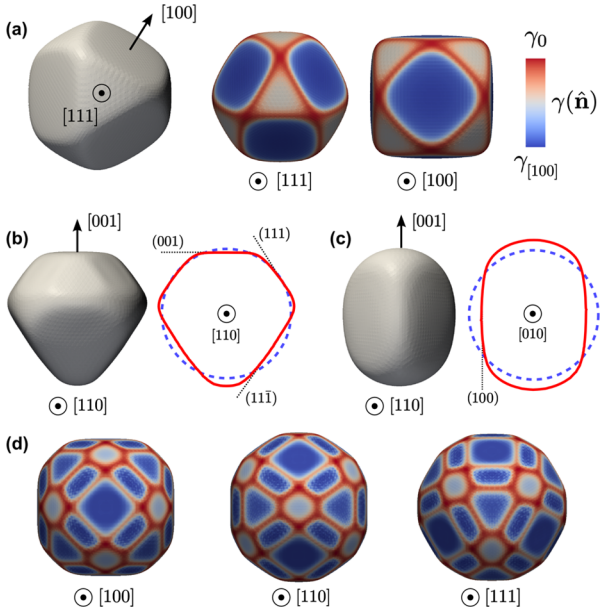

Figure 6. ECSs obtained by arbitrary tuning of the $\gamma(\hat{\mathbf{n}})$. (a) As in Figure 4b with halved value of α_i along ⟨111⟩ directions. Perpective 3D view and $\gamma(\hat{\mathbf{n}})$ color map are shown. In (b) and (c) we show asymmetric shape with perspective 3D views and with comparisons in a central cross-section between the resulting shape and the initial spherical profile. Parameters in (b): [0 0 1], [±1 ±1 1], [±1 0 1], [0 ±1 1] minima directions with $\alpha_i = 0.2$ and $w_i = 60$, [±1 ±1 $\bar{1}$] minima directions with $\alpha_i = 0.4$ and $w_i = 30$, $\beta = 0.002$. Parameters in (c): minima along [± 1 0 0] and [0 ± 1 0] with $\alpha_i = 0.4$, $w_i = 10$, $\beta = 0.002$. (d) Shape of a Ge crystal including {001}, {110}, {111}, and {113} facets by considering energy minima as in ref 32 with $\beta = 0.003$, $w_i = 100$ for minima along ⟨113⟩ direction and $w_i = 50$ for the others, $\alpha_{\{001\}} = 0.3$.

This makes our method suitable to investigate realistic systems which exhibit ECS-like structures, such as those shown in refs 1−3 (where some morphologies recall the ones obtained so far). An example where we reproduce a specific realistic morphology is illustrated in Figure 6d, where theoretical data for Ge surface energy[32] are used to set $\gamma(\hat{\mathbf{n}})$ and predict the corresponding ECS. Furthermore, another important application may consist of matching simulated ECS with experimental shapes in order to obtain estimates of $\gamma(\hat{\mathbf{n}})$.

Morphologies of Long-Lived, Metastable Structures. The ECS can be considered as the ideal state providing the global minimization of the surface energy. However, the outcome of experiments may not correspond to it because of the presence of sufficiently long-lived metastable, or kinetically frozen out-of-equilibrium states. Present nanoscience and nanotechnology widely exploit structures which do not correspond to a global minimum in the phase-space (quantum dots or nanowires being only two possible examples), as they can display a peculiar behavior, absent in the lowest free-energy state. Faceting of morphologies not corresponding to global equilibrium can be described by suitable cutting of the ECS, or by specific modifications in the Wulff construction procedure,[13,33] but care is needed in extracting actual details of $\gamma(\hat{\mathbf{n}})$ by a simple comparison between model and experiments, particularly when one is willing to account for the temporal evolution of a faceted crystal.

A more appropriate description should be based on a unique definition of $\gamma(\hat{\mathbf{n}})$ from experimental data at equilibrium (or from theoretical calculations as in Figure 6d). Deviations from the ECS could then be explained by considering the initial out-of-equilibrium geometry and taking into account the time evolution of the profile, driven by its tendency to the equilibrium. Our approach allows us to tackle this additional degree of complexity as it does not consist of a simple minimization of the surface energy but provides the whole evolution path toward it. In the following, we focus our attention on a few peculiar nanostructure morphologies, by setting $\gamma(\hat{\mathbf{n}})$ from data in the literature and considering suitable initial profiles. As we shall show, the simulation results nicely match the experimental morphologies referred to in the literature.

Homoepitaxial islands[34] or top-down designed patterns produced by lithography[35] belong to the description discussed above as their shape can be substantially different from the equilibrium configuration according to the specific fabrication processing. For the sake of simplicity, we set the minimum energy directions in $\gamma(\hat{\mathbf{n}})$, but we assume the same α_i (large enough to obtain sharp facets) and w_i. Figure 7 shows simulations reproducing the morphology of an island (in panels a and b) and of a pit-patterned substrate (in panel c). Here, the interface thickness is set equal to 0.1. More precisely, the island morphology is obtained starting from a half ellipsoidal shape intersecting a plane below which $\varphi = 1$ (for half of the cubic domain), as shown in Figure 7a, with an height-to-base aspect-ratio of 0.35 (in agreement with experimental ones[34]), and a lateral size equal to 2.4. The surface energy minima orientations are set according to theoretical data for GaAs.[36,37] The evolution of such an initial configuration, reported in Figure 7a, shows different faceted island structures resulting from different stages of the surface diffusion evolution. Notice that all these structures correspond to metastable configurations, as the final state would be the flat surface. The shape obtained at $t = 4.0$, characterized in Figure 7b, closely matches the morphology of GaAs nanometric islands observed in experiments, as in ref 34, where very similar island profiles can be found. The simulation of a pit geometry illustrated in Figure 7c is obtained

DOI: 10.1021/acs.cgd.5b00165
Cryst. Growth Des. 2015, 15, 2787−2794

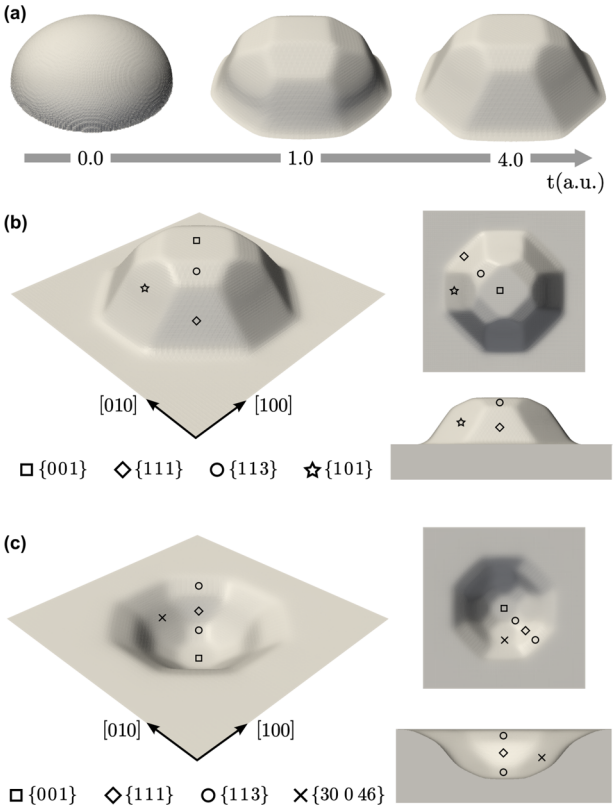

Figure 7. Faceting of structures on surfaces. (a) Evolution from the initial configuration (half-ellipsoidal) by including [0 0 1], [±1 ±1 1], [±1 ±1 3], [±1 0 1], and [0 ±1 1] minima directions,[36,37] $\alpha_i = 0.3$, $\beta = 0.006$. w_i are set as in Figure 6d. (b) Detailed view of the $t = 4.0$ stage of the evolution in panel (a) revealing an island faceting similar to the one obtained with GaAs in ref 34. (c) Faceting reproducing the one occurring in Si pit-patterned substrates as in ref 35 obtained by imposing minima at [0 0 1], [±1 ±1 1], [±1 ±1 3], [±30 0 46] and [0 ±30 46] directions,[32] $\alpha_i = 0.3$, $\beta = 0.006$. w_i are set as in Figure 6d and $w_{\{30\ 0\ 46\}} = 100$.

by considering a pit with a flat (001) surface at the bottom and a smooth connection with the surrounding flat substrate as initial profile. The pit aspect-ratio is set to 0.3, to reproduce a typical pit morphology resulting from etching,[38] with a lateral size of 2. The $\gamma(\hat{\mathbf{n}})$ minima orientations are set to reproduce the Si minimum energy surfaces.[32] ⟨30 0 46⟩ minima directions are considered in order to mimic neighboring {15 3 23} facets (e.g., [15 ±3 23]) recognized in experiments. Also in this case, the results closely resemble the experimental morphology of pit-patterned Si(001) substrates reported in refs 35 and 38. The good match achieved in Figure 7 is granted by setting an initial profile compatible with the experimental one. Indeed, different morphologies could be obtained with the same conditions but with different initial shapes and/or aspect-ratios.

Low-dimensional systems and elongated shapes can be considered as well as nonequilibrium structures as their shapes result from the growth mechanisms and are not due to extreme differences in their $\gamma(\hat{\mathbf{n}})$ minima. Also in these cases, our modeling is effective to describe the main morphological features. Examples are shown in Figure 8, where realistic nanowires are reproduced by means of surface diffusion evolution starting from a simplified parallelepiped shape, placed with the base in contact with the domain boundary in order to mimic the continuation of the lateral facets. In Figure 8a the morphology of a Ge nanowire grown along the [1 1 0]

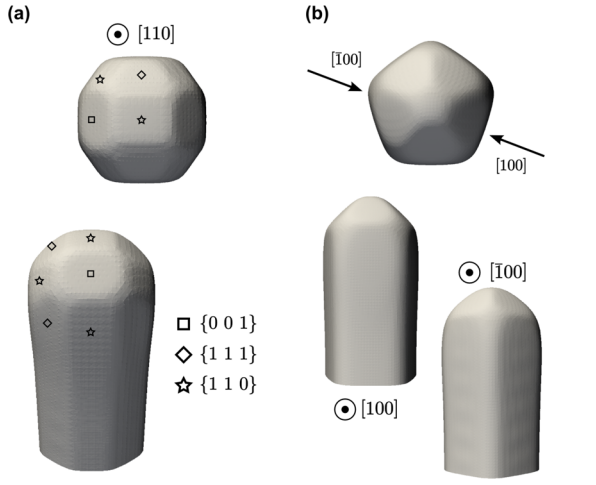

Figure 8. Morphology of far-from-equilibrium elongated shapes. (a) [1 1 0] Ge nanowire morphology including {100}, {110}, and {111} facets as in ref 5, obtained by selecting minima energy ratio of the Ge crystal[32] and $\alpha_{[001]} = 0.15$. (b) Ag nanowire with pentagonal symmetry[39] obtained by considering $\gamma(\hat{\mathbf{n}})$ in an effective way with minima along [sin(2 i π/5) cos(2i π/5) 0] and [sin(2 i π/5) cos(2 i π/5) 1] directions with $0 \leq i \leq 4$, $\alpha_i = 0.15$, $w_i = 30$, $\beta = 0.002$.

direction is reproduced, closely resembling the experimental structures reported in ref 5, including both top and sidewalls faceting. $\gamma(\hat{\mathbf{n}})$ values are selected according to the data reported in ref 32 for the energy minima along the ⟨100⟩, ⟨110⟩, and ⟨111⟩ directions. Another example is provided in Figure 8b, where the morphology of an Ag nanowire with pentagonal symmetry, reported in ref 39, is well matched by simulations. This peculiar experimental morphology results from twinning of five single crystal subunits exposing only {111} facets, so that the selected 5-fold $\gamma(\hat{\mathbf{n}})$ minima are not meant to reproduce the anisotropy of a single Ag crystal, but include the rotation around the nanowire axis of each subunit. Notice that the elongation of the morphologies shown in Figure 8 directly result from the definition of the initial profiles and not from a tuning of $\gamma(\hat{\mathbf{n}})$ as done in Figure 6c.

So far we considered systems where the evolution dynamics consisted only in a rearrangement of facets. Different initial conditions can however lead to more dramatic effects changing the topology of the system. This happens for instance in solid-state dewetting phenomena,[40−42] where separation occurs in a few subunits, leading to a local energy minimum. This metastable state can be reproduced only when considering a kinetic pathway not leading to the global energy minimization. Illustrative simulations reporting a similar mechanism are shown in Figure 9, where the evolution of an initial high aspect-ratio paralleleliped, completely embedded in the $\varphi = 0$ phase, is considered. Surface diffusion induces a strong flow of material toward the borders up to the separation of the initial profile in two distinct crystals, an outcome which is clearly far from the ECS. The occurrence of such a dramatic change in the morphology, is directly determined by the aspect-ratio of the initial configuration.[21] As shown by the simulations, this happens for both isotropic and anisotropic surface energy density (in the latter case $\gamma(\hat{\mathbf{n}})$ is set as in Figure 5a with $\alpha_i = 0.2$). Notice that such a dynamics is naturally included in the PF description,[21] thus representing an advantage over other methods, allowing topological changes to be simulated also in the case of highly anisotropic surface energy density.

DOI: 10.1021/acs.cgd.5b00165
Cryst. Growth Des. 2015, 15, 2787−2794

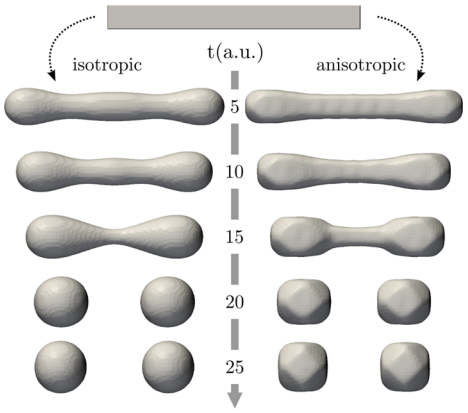

Figure 9. Surface diffusion evolution of a parallelepiped shape with of isotropic (left) and anisotropic (right) $\gamma(\hat{\mathbf{n}})$, the latter as in Figure 5a with $\alpha_i = 0.2$.

CONCLUSIONS

In this work we have introduced a convenient definition of an orientation-dependent surface energy, which, when considered together with a proper regularization term and implemented within a suitable PF framework, allows one to obtain arbitrary faceted shapes by surface diffusion. If no free-energy barriers are present, our approach leads, for long-enough evolution times, to the ECS corresponding to the Wulff construction. However, the main advantage stems from the possibility of describing faceting on out-of-equilibrium shapes, resulting in their time-dependent morphological evolution, eventually leading to a local free-energy minimum. In both cases, however, the simulations offer a description of the kinetic path from the initial to the final state thus describing the material flow in the out-of-equilibrium condition, resulting in a deeper understanding of such mechanisms in real systems.

Applications to relevant metastable nanostructures such as nanowires or dots were illustrated, revealing several features observed in experiments and pointing out the importance of the initial configuration in determining the observed facets extension in long-lived metastable states. In particular, the possibility to handle features at the nanoscale could be of great importance to provide coarse-grained investigations of a few tens of nanometers wide crystals, not directly accessible by atomistic calculations. Indeed, the model can be in principle applied to any size scale, provided that a continuum description exists and $\gamma(\hat{\mathbf{n}})$ is defined.

Importantly, the here provided methodology can be extended to other PF models tackling additional energy contributions affecting the profile evolution, such as elasticity,[44] intermixing effects for alloys and multicomponent systems,[45] as well as peculiar boundary conditions, e.g., contact angles at the interface of two materials.[46] The implementation of such further contributions would result in an unprecedented ability in modeling the time-evolution of complex nanostructures.

ASSOCIATED CONTENT

Supporting Information

Details about the anisotropy regime assessment and the explicit integration scheme adopted in the PF simulations. The Supporting Information is available free of charge on the ACS Publications website at DOI: 10.1021/acs.cgd.5b00165.

AUTHOR INFORMATION

Corresponding Authors

*(M.S.) E-mail: marco.salvalaglio@mater.unimib.it.
*(F.M.) E-mail: francesco.montalenti@unimib.it.

Notes

The authors declare no competing financial interest.

ACKNOWLEDGMENTS

The strong need for a model that is able to tackle faceting of realistically shaped metastable structures was first pointed out to us by Prof. Leo Miglio. This work was partially supported by the Cariplo Foundation (DEFCON-IV project). R.Ba. and A.V. acknowledge support from the German Science Foundation within SPP 1296 Vo899/7 and EXC CfAED as well as the European Commission within FP7-PEOPLE-2009-IRSES PHASEFIELD. Simulations were carried out at ZIH at TU Dresden and JSC at FZ Jülich.

REFERENCES

(1) Sun, Y. G.; Xia, Y. N. *Science* **2002**, *298*, 2176−2179.
(2) Tao, A. R.; Habas, S.; Yang, P. *Small* **2008**, *4*, 310−325.
(3) Barnard, A. S.; Young, N. P.; Kirkland, A. I.; van Huis, M. A.; Xu, H. *ACS Nano* **2009**, *3*, 1431−1436.
(4) Medeiros-Ribeiro, G.; Bratkovski, A. M.; Kamins, T. I.; Ohlberg, D. A. A.; Williams, R. S. *Science* **1998**, *279*, 353−355.
(5) Hanrath, T.; Korgel, B. A. *Small* **2005**, *1*, 717−721.
(6) Falub, C. V.; von Känel, H.; Isa, F.; Bergamaschini, R.; Marzegalli, A.; Chrastina, D.; Isella, G.; Müller, E.; Niedermann, P.; Miglio, L. *Science* **2012**, *335*, 1330−1334.
(7) Bergamaschini, R.; Isa, F.; Falub, C. V.; Niedermann, P.; Müller, E.; Isella, G.; von Känel, H.; Miglio, L. *Surf. Sci. Rep.* **2013**, *68*, 390−417.
(8) An, Q.; Dong, C.; Zhu, W.; Tao, C.; Yang, H.; Wang, Y.; Li, G. *Small* **2012**, *8*, 562−568.
(9) Auyeung, E.; Li, T. I. N. G.; Senesi, A. J.; Schmucker, A. L.; Pals, B. C.; Olvera de la Cruz, M.; Mirkin, C. A. *Nature* **2014**, *505*, 73−77.
(10) Wulff, G. *Z. Kristallogr.* **1901**, *34*, 449−530.
(11) Herring, C. *Phys. Rev.* **1951**, *82*, 87−93.
(12) Roosen, A. R.; McCormack, R. P.; Carter, W. C. *Comput. Mater. Sci.* **1998**, *11*, 16−26.
(13) Zucker, R. V.; Chatain, D.; Dahmen, U.; Hagege, S.; Carter, W. C. *J. Mater. Sci.* **2012**, *47*, 8290−8302.
(14) Scopece, D. *J. Appl. Crystallogr.* **2013**, *46*, 811−816.
(15) Pimpinelli, A., Villain, J. In *Physics of Crystal Growth*; Cambridge University Press: Cambridge, UK, 1998.
(16) Frank, F. On the Kinematic Theory of Crystal Growth and Dissolution Processes In *Growth and Perfection in Crystals*; Doremus, R. H., Roberts, B. W., Turnbull, D., Eds.; Wiley: New York, 1958; pp 411−419.
(17) Chernov, A. A. *Sovi. Phys. Crystallogr.* **1963**, *7*, 728−730.
(18) Shaw, W. *J. Cryst. Growth* **1979**, *47*, 509−517.
(19) Mullins, W. W. *J. Appl. Phys.* **1957**, *28*, 333−339.
(20) Carter, W. C.; Roosen, A. R.; Cahn, J. W.; Taylor, J. E. *Acta Metall. et Mater.* **1995**, *43*, 4309−4323.
(21) Li, B.; Lowengrub, J.; Ratz, A.; Voigt, A. *Commun. Comput. Phys.* **2009**, *6*, 433−482.
(22) Spencer, B. J. *Phys. Rev. E* **2004**, *69*, 011603.
(23) Eggleston, J. J.; McFadden, G. B.; Voorhees, P. W. *Physica D* **2001**, *150*, 91−103.
(24) Gurtin, M. In *Thermodynamics of Evolving Phase Boundaries in the Plane*; Oxford University Press: Oxford, U.K., 1993.
(25) Vey, S.; Voigt, A. *Comput. Visual. Sci.* **2007**, *10*, 57−67.
(26) Witkowski, T.; Ling, S.; Praetorius, S.; Voigt, A. *Adv. Comput. Math.* **2015**, DOI: 10.1007/s10444-015-9405-4.
(27) Torabi, S.; Lowengrub, J.; Voigt, A.; Wise, S. *Proc. R. Soc. A* **2009**, *465*, 1337−1359.

DOI: 10.1021/acs.cgd.5b00165
Cryst. Growth Des. 2015, 15, 2787−2794

(28) Cahn, J. W.; Hilliard, J. E. *J. Chem. Phys.* **1958**, *28*, 258−267.
(29) Du, Q.; Liu, C.; Ryham, R.; Wang, X. *Nonlinearity* **2005**, *18*, 1249−1267.
(30) Siem, E. J.; Carter, W. C. *J. Mater. Sci.* **2005**, *40*, 3107−3113.
(31) Sekerka, R. F. *J. Cryst. Growh* **2005**, *275*, 77−82.
(32) Stekolnikov, A. A.; Bechstedt, F. *Phys. Rev. B* **2005**, *72*, 125326.
(33) Winterbottom, W. L. *Acta Metall.* **1967**, *15*, 303−310.
(34) Wong, P. S.; Liang, B. L.; Moleke, R.; Tatebayashi, J.; Huffaker, D. L. *Cryst. Growth Des.* **2010**, *10*, 2509−2014.
(35) Zhang, J. J.; Stoffel, M.; Rastelli, A.; Schmidt, O. G.; Jovanovic, V.; Nanver, L. K.; Bauer, G. *Appl. Phys. Lett.* **2007**, *91*, 173115.
(36) Moll, N.; Kley, A.; Pehlke, E.; Scheffler, M. *Phys. Rev. B* **1996**, *54*, 8844−8855.
(37) Platen, J.; Kley, A.; Setzer, C.; Jacobi, K.; Ruggerone, P.; Scheffler, M. *J. Appl. Phys.* **1999**, *85*, 3597−3601.
(38) Bergamaschini, R.; Tersoff, J.; Tu, Y.; Zhang, J. J.; Bauer, G.; Montalenti, F. *Phys. Rev. Lett.* **2012**, *109*, 156101.
(39) Wiley, B.; Sun, Y.; Mayers, B.; Xia, Y. *Chem.—Eur. J.* **2005**, *11*, 454−463.
(40) Santala, M. K.; Glaeser, A. M. *Acta Mater.* **2008**, *56*, 1967−1980.
(41) Capellini, G.; Ciasca, G.; De Seta, M.; Notargiacomo, A.; Evangelisti, F.; Nardone, M. *J. Appl. Phys.* **2009**, *105*, 093525.
(42) Ye, J.; Thompson, C. V. *Adv. Mater.* **2011**, *23*, 1567−1571.
(43) Karma, A.; Rappel, W. J. *Phys. Rev. E* **1998**, *57*, 4323−4349.
(44) Rätz, A.; Ribalta, A.; Voigt, A. *J. Comput. Phys.* **2006**, *214*, 187−208.
(45) Backofen, R.; Bergamaschini, R.; Voigt, A. *Philos. Mag.* **2014**, *94*, 2162−2169.
(46) Jiang, W.; Bao, W.; Thompson, C. V.; Srolovitz, D. J. *Acta Mater.* **2012**, *60*, 5578−5592.

DOI: 10.1021/acs.cgd.5b00165
Cryst. Growth Des. 2015, 15, 2787−2794